STM JOURNALS

Journal of
Polymer & Composites

ISSN: 2321-2810 (Online)
ISSN: 2321-8525 (Print)
Volume 13, Issue 6, 2025
DOI (Journal): 10.37591/JoPC

https://journals.stmjournals.com/jopc

Research JoPC

Graphene-Derived Reinforced Polymer Composites for Self-Healing and Durability Enhancement in Concrete Structures

V. Ravi Raj[1*], Neethi Madhavan C.S[2], Bikash Chandra Saha[3], Manu Vijay[4], D. Sudha[5], S. Sivakumar[6], R. M. Karthikeyan[7], Shailendra Kumar Bohidar[8], Zakir Hussain[9]

Abstract

This study presents a matrix-centric polymer-composite repair binder: an epoxy–polyamide network reinforced with graphene derivatives (GO/rGO, 0.1–1.0 wt%). The polymer drives function via segmental mobility that closes microcracks, while 2D-filler topology densifies the interphase, improves load transfer, and enforces tortuous moisture pathways. Adhesion was high: pull-off (ASTM D4541) reached 13.5 MPa at 2.0 mm displacement; slant-shear (ASTM C882) reached 12.1 MPa at 2.8 mm, with greater deformation capacity (zero stress ~5.6 mm) and higher work-to-failure (~45.17 MPa·mm) than pull-off (~36.00 MPa·mm), evidencing polymer ductility and filler-mediated bridging under mixed-mode loading. Water permeability (EN 12390-8, 0.5 MPa, 72 h) plateaued at ~7.3 mm, with average ingress rates dropping from ~0.236 to ~0.053 to ~0.015 mm h^{-1} across 0–24, 24–48, and 48–72 h, consistent with pore blocking and microcrack self-sealing within the composite interphase. Pre-cracked specimens (~0.2 ± 0.05 mm) recovered ~35% strength by day 1, ~78% by day 5, and ~92% by day 7 at 25 °C/60% RH, confirming polymer-enabled healing assisted by filler percolation across crack wakes. SEM revealed uniform filler dispersion, polymer fibrils bridging microcracks, and a dense, low-void interphase; EDS and mapping indicated O (~40 wt%), Si (~25 wt%), Ca (~15 wt%), and C (~20 wt%) with Si-rich streaks along crack corridors. Overall, this polymer-composite binder couples high adhesion, low permeability, and autonomous healing to extend durability under wet or cyclic service.

Keywords: Polymer-composite, graphene, adhesion, micro-cracks, self-healing

***Author for Correspondence**
V. Ravi Raj
Email: raviraj.mech@sairam.edu.in

[1]Associate Professor, Department of Mechanical Engineering, Sri Sairam Engineering College, Chennai, Tamil Nadu, India
[2]Assistant Professor, Department of Aeronautical Engineering, Rajadhani Institute of Engineering and Technology, Kerala, India
[3]Associate Professor, Department of Electrical and Electronics Engineering, Cambridge Institute of Technology, Ranchi, Jharkhand, India
[4]Associate Professor, Department of Civil Engineering, ATME College of Engineering, Mysore, Karnataka, India
[5]Associate Professor, Department of Physics, R.M.K. Engineering College, Tamil Nadu, India
[6]Professor, Department of Chemistry, Varuvan Vadivelan Institute of Technology, Dharmapuri, Tamil Nadu, India
[7]Associate Professor, Department of Civil Engineering, SNS College of Technology, Coimbatore, Tamil Nadu, India
[8]Associate Professor, Department of Mechanical Engineering, School of Engineering & I.T, MATS University, Raipur, Chhattisgarh, India
[9]Assistant Professor, Department of Chemical Technology, Loyola Academy, Secunderabad, Telangana, India

Received Date: August 22, 2024
Accepted Date: September 03, 2025
Published Date: September 13, 2025

Citation: V. Ravi Raj, Neethi Madhavan C.S., Bikash Chandra Saha, Manu Vijay, D. Sudha, A. Sivakumar, R. M. Karthikeyan, Shailendra Kumar Bohidar, Zakir Hussain. Graphene-Derived Reinforced Polymer Composites for Self-Healing and Durability Enhancement in Concrete Structures. Journal of Polymer & Composites. 2025; 13(6): S77–S91p.

INTRODUCTION

Concrete remains the structural backbone of global infrastructure, with annual production exceeding ten billion tonnes, yet its quasi-brittle nature makes it intrinsically vulnerable to cracking under mechanical loading, drying shrinkage, freeze–thaw cycling, and combined environmental actions [1]. In service, even sub-critical micro-cracks become transport highways for aggressive agents—chlorides, CO_2, and sulphates—that infiltrate the pore network, lower alkalinity, disrupt passivation, and initiate corrosion and other chemomechanical deterioration pathways, ultimately truncating service life and increasing

life-cycle cost [2]. Chloride-induced corrosion, in particular, has been documented as a dominant cause of premature distress in reinforced concrete (RC) bridge decks, translating into recurrent, multi-billion-dollar maintenance burdens that strain asset managers and public budgets [3]. Against this background, polymer-composites offer a compelling material system to address the coupled challenges of crack control, transport resistance, and interfacial integrity at concrete repair interfaces. Unlike monolithic binders, polymer-composites integrate a polymer matrix with reinforcing particulates or fibres to deliver a designed suite of mechanical, chemical, and barrier properties tailored to the harsh chemo-physical milieu of concrete service environments [5]. The polymer matrix in polymer-composites enables strong adhesion, wetting of rough, porous substrates, low shrinkage, and chemical resistance, while the dispersed reinforcement in polymer-composites tunes stiffness, fracture energy, and transport tortuosity, enabling multifunctional performance unattainable with conventional repair mortars alone [5].

Traditional repair strategies—including cementitious overlays, epoxy injections, and polymer-modified mortars—have advanced field practice yet remain constrained by interface debonding, thermo-mechanical mismatch, moisture sensitivity, and the recurrence of cracking under cyclic or differential movements [4]. In such systems, the repair layer is often passive: it may resist damage to a point, but once microcracks form, there is no intrinsic pathway to recover stiffness or close transport channels. Repeated crack–repair–recrack cycles lead to interphase degradation, porosity at the interface, and loss of composite action with the parent concrete—all failure modes that polymer-composites must be engineered to prevent or actively mitigate [4]. Because the concrete–repair junction is governed by mechanics (stress transfer, constraint), thermodynamics (wetting, adhesion), and transport (moisture/ion ingress), a systems approach is needed; polymer-composites embody that approach by allowing the interphase to be molecularly and microstructurally designed for adhesion, toughness, and barrier function simultaneously [5]. In practice, polymer-composites fashioned from epoxies, polyurethanes, or vinyl esters, combined with silicate, carbon, or hybrid nanofillers, can infiltrate surface asperities, anchor into the cementitious microtexture, and form a continuous, low-void interphase. This polymer-composites interphase distributes shear/peel stresses, blunts flaw tips, bridges microcracks, and lengthens transport pathways, thereby elevating durability indices beyond the sum of the individual constituents [5].

Within the last two decades, a paradigm has emerged in which polymer-composites are not only robust but also functional—able to sense, adapt, or heal damage in situ [6–8]. Self-healing polymer-composites are inspired by biological analogues where damage triggers autonomous repair, and they are broadly classed as intrinsic or extrinsic systems [7]. Intrinsic self-healing polymer-composites rely on dynamic covalent chemistries or supramolecular interactions that—when activated by heat, moisture, or light—permit chain mobility, bond exchange, and re-entanglement, leading to partial or near-complete restoration of load transfer [8]. Extrinsic self-healing polymer-composites embed microcapsules or vascular networks that release healing agents upon crack rupture, re-bonding faces and sealing transport channels [8]. For coating-like applications, capsules are effective but offer finite reservoirs; by contrast, intrinsic polymer-composites enable repeatable healing cycles provided the matrix retains mobility and activation stimuli can reach the interphase [9]. The performance ceiling of both classes is lifted when nanofillers are introduced, because nanofillers enhance the micromechanics of polymer-composites (stress transfer, crack-bridging) and their mesoscopic transport behavior (tortuosity, percolation) [9–11]. In short, polymer-composites provide a scaffold for integrating healing chemistries with reinforcement topology so that the same material that resists cracking can also assist in closing it.

Nanomaterials—owing to extreme surface-to-volume ratios, high intrinsic stiffness/strength, and tunable surface chemistries—have transformed the design space of polymer-composites [10]. In polymer-composites, nanoparticles increase modulus, elevate yield strength, and—critically for quasi-brittle concrete interfaces—raise fracture energy via mechanisms such as crack deflection, crack

pinning, pull-out, and plastic zone enlargement [10,11]. Equally important, the same nanofillers induce barrier tortuosity in polymer-composites, making the path for water, oxygen, and chloride ions longer and more circuitous, thereby lowering effective diffusivity without sacrificing processability [10]. Tailored nanofillers also enable polymer-composites to acquire functional properties—electrical/thermal conductivity for Joule- or photothermal-assisted healing, or chemical affinity for scavenging deleterious species—that are otherwise inaccessible in neat polymers [11]. Among carbonaceous nanofillers, graphene derivatives align particularly well with the multifunctional aspirations of polymer-composites because they combine atomically thin morphology with exceptional modulus and strength, and because their surface chemistries can be engineered to couple strongly to common thermoset matrices [12].

Graphene oxide (GO) and reduced graphene oxide (rGO) have therefore become mainstays in advanced polymer-composites for civil infrastructure applications [12,13]. GO offers oxygen-bearing groups (hydroxyl, epoxy, carboxyl) that hydrogen-bond or react with polar epoxy networks, while rGO, with fewer oxygen functionalities, provides higher stiffness and electrical conductivity—attributes valuable for electro-stimulated healing and robust load transfer in polymer-composites [13]. Because of their two-dimensional geometry and extreme aspect ratio, graphene sheets form percolated or quasi-percolated networks at sub-percent loadings, endowing polymer-composites with enhanced fracture resistance, elastic modulus, and damage tolerance without incurring the viscosity penalties typical of spherical or short-fiber fillers [13]. Mechanistically, graphene sheets act as nano-bridges in polymer-composites, spanning nascent crack planes and forcing cracks to kink, branch, or arrest; simultaneously, their impermeability increases tortuosity, lowering permeability and suppressing chloride ingress—benefits that are particularly potent at the concrete interphase where wetting–drying and salt exposure drive durability loss [14]. In this sense, graphene-enhanced polymer-composites collapse multiple functional targets—toughening, barrier, and healing—into a single material architecture.

The functionality of graphene-modified polymer-composites extends beyond the polymer bulk into the cementitious substrate–binder interphase, where performance is often decided [15]. GO's hydroxyl and carboxyl groups can interact with calcium silicate hydrate (C–S–H) via hydrogen bonding or ionic coordination, increasing interphase cohesion and frictional resistance, while rGO promotes mechanical interlocking within the microroughness of the cement paste and, by being more hydrophobic, contributes to moisture exclusion at the interface [15]. The result is an ITZ (interfacial transition zone) in which polymer-composites exhibit reduced porosity, tighter crack opening displacements, and improved stress transfer under combined shear/peel. Such interphase consolidation in polymer-composites mitigates the classic weak-link behavior of overlays and sealants, elevating both peak adhesion and energy absorption capacity when compared against unmodified binders [15]. In chloride-rich or cyclic wet environments, these combined effects—nano-bridging, interphase densification, and hydrophobic sealing—allow polymer-composites to sustain service longer before initiation of corrosion or delamination [14,15]. Thus, graphene-enabled polymer-composites are not only stronger but smarter, as their microstructure is tailored to the dominant degradation modes at concrete surfaces.

Despite the promise, critical gaps remain in translating graphene-enhanced polymer-composites into field-ready, smart interfacial binders for concrete [16]. Much of the literature demonstrates barrier improvement or mechanical strengthening in isolation; far fewer studies benchmark polymer-composites that jointly deliver high adhesion, low permeability, and autonomous healing in alkali, wet, and cyclic thermal conditions representative of real cementitious environments [16]. Moreover, the benefits of GO/rGO in polymer-composites depend sensitively on dispersion quality and optimized loading. Below ~0.5 wt% GO, barrier properties can improve markedly, yet achieving simultaneous gains in adhesion, crack healing, and long-term durability in polymer-composites often requires dual-filler strategies (GO + rGO) and surfactant/functionalization routes that avoid agglomeration and viscosity spikes [16]. Poor dispersion in polymer-composites produces stress concentrators that undermine fracture resistance and open transport channels—exactly the weaknesses the materials were

intended to eliminate. There is thus a clear need for protocols that balance percolation for mechanical/transport benefits against processing realities for polymer-composites (pot life, coatability, cure), especially in field-applied repair contexts where surface moisture and temperature fluctuate.

In addition to formulating polymer-composites with tuned chemistry and filler topology, rigorous, interface-specific characterization is essential. Adhesion must be interrogated with mixed-mode and pure-tension methods (e.g., slant shear and pull-off), because polymer-composites at concrete interfaces experience combined shear and peel in service [4,5]. Transport must be quantified under hydrostatic gradients and cyclic exposure to verify that polymer-composites actually suppress ingress over relevant timescales [2,3]. Healing must be probed with controlled pre-cracks and environmental conditioning to confirm that polymer-composites can recover strength repeatedly under realistic humidity and temperature ranges [6–9]. Finally, microstructural evidence—SEM of crack-bridging ligaments, EDS spectra and elemental maps of interphase chemistry—should corroborate macroscopic performance and reveal whether polymer-composites create the anticipated "filler corridors" along crack paths that provide both load-transfer rails and capillary occlusion [10–15]. Such correlative evidence is crucial to convince practitioners and reviewers that improvements stem from designed polymer-composites mechanisms rather than test artefacts.

Against this backdrop, the present work advances a polymer-composites-centered strategy for concrete interface repair. We design epoxy-based polymer-composites reinforced with graphene derivatives (GO, rGO) expressly for interfacial use, so that the interphase is not a passive weak zone but an active, multifunctional layer that spreads stresses, heals microcracks, and blocks water/ion ingress [5–9,12–15]. The approach views the interface as a composite in its own right: a graded region where polymer-composites chemistry, segmental dynamics, and 2D filler topology are exploited to achieve multiple objectives at once. First, we target adhesion by leveraging wetting and mechanical interlocking plus nanoscale crack-bridging in polymer-composites to raise both peak strength and work-to-failure. Second, we attack transport by maximising tortuosity in polymer-composites via percolated graphene networks that lengthen diffusion paths and promote self-sealing. Third, we embed repeatable, stimulus-assisted healing into polymer-composites, using the polymer's mobility and filler-mediated heat/electro-thermal pathways to encourage crack closure before macro-defects propagate [6–9,11–13]. This triad—adhesion, barrier, healing—defines the performance envelope of polymer-composites in a way that aligns with actual deterioration modes in RC structures.

The specific scientific questions we address are: (i) How do GO/rGO loading and dispersion state tune the balance between stiffness, fracture energy, and adhesion in epoxy polymer-composites bonded to concrete? (ii) To what extent can polymer-composites reduce water ingress under hydrostatic head over multi-day exposures, and can the early-time ingress be throttled by microcrack sealing? (iii) Can polymer-composites recover mechanical performance after controlled microcracking under ambient conditions, and what microstructural signatures (fibrils, bridges, re-deposited phases) accompany the recovery? (iv) Which elemental distributions at the interphase (e.g., Si-rich streaks, Ca distributions, C enrichment) correlate with transport suppression and adhesion gains in polymer-composites? By answering these, we aim to ground the case for polymer-composites as smart, durable, and field-viable binders for infrastructure repair.

Methodologically, we combine standardized mechanical tests with transport and microstructural assays germane to polymer-composites at concrete interfaces. Mixed-mode slant shear (ASTM C882) and pull-off (ASTM D4541) reveal how polymer-composites carry load under shear-dominant and peel-dominant conditions, respectively, while comparing peak strength and energy absorption clarifies ductility contributions from crack-bridging and interphase plasticity [4,5]. Hydrostatic permeability (EN 12390-8) quantifies how polymer-composites throttle water penetration and whether early-time ingress decelerates as microchannels are occluded by filler corridors or polymer reflow [2]. Healing metrics, based on pre-cracked beams held at realistic humidity/temperature, expose the kinetics of

strength recovery in polymer-composites and test the repeatability of intrinsic healing aided by the nanofiller network [6–9]. SEM provides direct evidence of polymer fibrils and bridging ligaments in polymer-composites; EDS spectra and elemental maps track Si/Ca/O/C distributions across crack corridors and interphase zones, clarifying how polymer-composites restructure the ITZ and reduce connected porosity [10–15]. Together, these techniques tie macroscopic performance to designed polymer-composites mechanisms, ensuring that claims are mechanistically anchored.

From a practical perspective, the value proposition of polymer-composites is not only enhanced performance but also constructability. Formulations must exhibit workable viscosity/gel time for field application, bond well to moist or variably conditioned concrete, and cure to stable performance under fluctuating temperatures—criteria that polymer-composites are uniquely suited to meet via resin selection and filler surface tailoring [5]. Epoxy-based polymer-composites can be tuned with diluents, toughening, and coupling agents, while GO/rGO can be functionalized to control dispersion and interfacial adhesion, yielding robust, repeatable rheology and cure behaviour compatible with site constraints [13,16]. When correctly formulated, polymer-composites allow thin, conformal, and defect-lean coatings or interlayers that are resilient under shear and peel, resistant to water and chlorides, and capable of partial performance recovery after microcracking—capabilities that align directly with maintenance objectives for bridges, coastal assets, parking structures, and water retaining systems.

In summary, the trajectory from passive to functional repair materials points decisively toward polymer-composites that unite adhesion, barrier function, and autonomous healing in one interphase architecture. The literature has charted each axis—mechanical reinforcement, transport suppression, and healing—yet integrated demonstrations in harsh cementitious environments remain sparse, and optimization of GO/rGO ratios and dispersion in polymer-composites is an unresolved, high-leverage problem [16]. The present work addresses these gaps by engineering graphene-reinforced polymer-composites to act as smart, durable interfacial binders for concrete; by benchmarking adhesion, permeability, and healing under standardized yet realistic conditions; and by elucidating the microstructural and chemical foundations by which polymer-composites achieve their multifunctionality. Through this lens, polymer-composites are not ancillary coatings but central, active components of infrastructure durability design—materials that transform the weakest link of a repair, the interface, into the strongest, most protective element of the system. Pilot-scale studies on bridge decks and marine concrete elements have validated reduced crack propagation and up to 40% lower chloride ingress with graphene-polymer coatings over a monitoring period of 2–3 years. However, long-term field data exceeding a decade are still limited, emphasizing the need for continued deployment and monitoring.

Experimental Section

Materials

The polymer matrix used in this study (Figure 1) comprised a bisphenol-A based epoxy resin (diglycidyl ether of bisphenol-A, DGEBA; viscosity 11,000 ± 500 mPa•s at 25 °C) and a polyamide curing agent (amine value 290–310 mg KOH/g).

Graphene oxide (GO) was synthesized in-house via a modified Hummers' method from natural graphite flakes (≥99% purity, 45 μm average size), yielding a C/O atomic ratio of approximately 2.1 and lateral sheet sizes of 2–5 μm. Reduced graphene oxide (rGO) was obtained by chemical reduction of GO using hydrazine hydrate (≥99%, Merck, India) at 95 °C for 24 h, achieving a C/O ratio of ~8.5 and restoring partial sp^2 domains.

Concrete substrates were prepared using Ordinary Portland Cement (OPC) 43-grade, river sand (fineness modulus 2.7), and coarse aggregate (maximum size 12 mm), with mixing water conforming to IS:456–2000 standards. Analytical-grade acetone (≥99.5%) was used as the solvent for graphene dispersion.

Figure 1. Materials used: epoxy resin, polyamide curing agent, graphene oxide, and reduced graphene oxide.

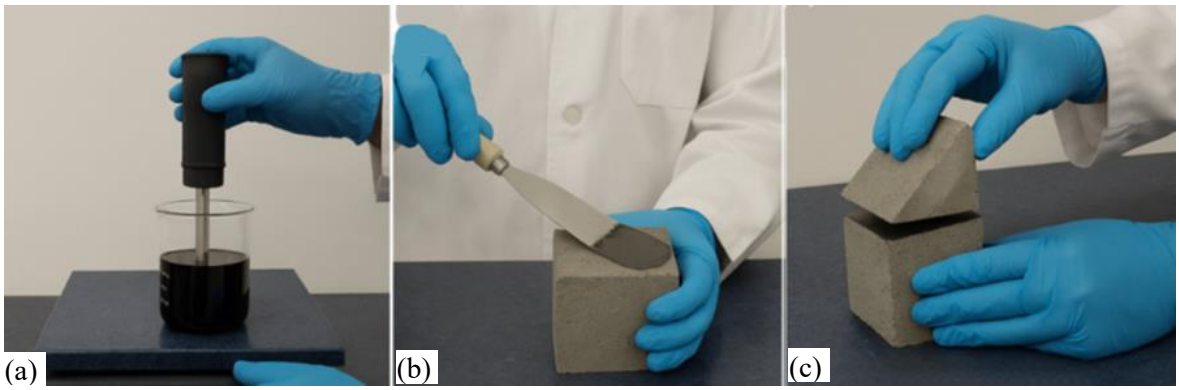

Figure 2. Preparation of graphene–polymer composite binders and concrete joint assembly. (a)Ultrasonication of graphene suspension in acetone for uniform dispersion. (b)Application of graphene–polymer composite binder onto prepared concrete surface. (c) Assembly of slant shear concrete joint for adhesion testing.

Synthesis of Graphene Derivatives

Graphene oxide (GO) was synthesized (Fig.2) via a modified Hummers' method in which 5 g of graphite flakes were dispersed in 115 mL of concentrated H_2SO_4 (98%) under ice-bath conditions (0–5 °C), followed by the addition of 2.5 g $NaNO_3$ and the slow introduction of 15 g $KMnO_4$ over 30 min. The mixture was then heated to 35 °C and stirred for 2 h to facilitate oxidation. Subsequently, 230 mL of deionized (DI) water was added gradually, increasing the temperature to 98 °C for 30 min, and the reaction was terminated by adding 700 mL DI water and 30 mL H_2O_2 (30%) until the solution turned bright yellow. Purification was carried out through repeated centrifugation–washing cycles with 5% HCl and DI water until the pH reached ~6, after which the product was freeze-dried at −50 °C for 48 h. Reduced graphene oxide (rGO) was obtained by dispersing 1 g of GO in 200 mL DI water via ultrasonication (150 W, 40 kHz) for 30 min, adding 2 mL hydrazine hydrate, and refluxing the mixture at 95 °C for 24 h, followed by filtration, washing, and freeze-drying.

Preparation of Graphene–Polymer Composite Binders

GO and rGO were individually dispersed in acetone at loadings of 0.1, 0.3, 0.5, 0.7, and 1.0 wt% relative to the epoxy resin mass. For dispersion, the graphene derivatives were first added to acetone

and ultrasonicated (150 W, 40 kHz) for 30 min in a bath sonicator to break up agglomerates. The resulting suspension was then added dropwise into epoxy resin under mechanical stirring at 1500 rpm for 10 min at 25 °C. Following mixing, the solvent was removed by degassing the mixture under vacuum (−0.08 MPa) for 15 min to evaporate acetone and eliminate trapped air bubbles. The polyamide curing agent was then introduced at a stoichiometric ratio of 100:12 (epoxy:hardener by weight) and gently mixed at 500 rpm for 5 min to prevent air entrapment. Finally, the prepared graphene–polymer binder systems were stored in airtight containers to prevent premature curing.

Concrete Substrate Preparation

Concrete blocks measuring 100 × 100 × 50 mm were cast using a 1:2.5:2.5 mix ratio of cement, sand, and aggregate, with a water-to-cement ratio of 0.45. The specimens were cured in water for 28 days to ensure complete hydration. Prior to binder application, the bonding surfaces were prepared by grinding with 120-grit SiC paper to remove surface laitance, cleaning with compressed air to eliminate dust particles, wiping with acetone-soaked lint-free cloths to promote surface activation, and finally storing in a desiccator to maintain dryness until use.

Binder Application and Joint Assembly

For mechanical adhesion testing, slant shear joints were fabricated in accordance with ASTM C882. A uniform binder layer of 0.8 ± 0.05 mm thickness was applied to the prepared concrete surface using a notched applicator. The concrete halves were then assembled and subjected to a compressive preload of 0.3 MPa for 5 min to ensure intimate interfacial contact. The assembled specimens were cured at 25 °C and 60% relative humidity for 24 h, followed by a post-curing step at 50 °C for 4 h to promote enhanced crosslinking of the polymer matrix.

Testing Procedures

Mechanical Adhesion Strength

- *Slant Shear Test:* ASTM C882 was followed. Specimens were loaded in a universal testing machine (Instron 5969) at a rate of 1 mm/min until failure.
- *Pull-Off Test:* ASTM D4541 was used. Dollies (20 mm diameter) were bonded to the composite layer with a two-part epoxy and tested using a pull-off adhesion tester (PosiTest AT-A, DeFelsko).

Water Permeability

EN 12390-8 was used to measure water penetration depth under 0.5 MPa hydrostatic pressure for 72 h. Penetration depths were measured after splitting the specimens.

Self-Healing Efficiency

Pre-cracks of 0.2 ± 0.05 mm were induced using a three-point bending setup. Specimens were stored at 25 °C and 60% RH for 7 days before retesting. Healing efficiency (%) was calculated as:

- Healing Efficiency = (Post-healing strength / Initial strength) × 100

Microstructural Analysis

- *SEM:* Hitachi S-4800 field-emission SEM was used to examine filler dispersion, crack-bridging, and interphase morphology.
- *EDS:* Energy-dispersive X-ray spectroscopy confirmed elemental composition and filler localization at the interface.

RESULTS AND DISCUSSION

Mechanical Adhesion Strength

The adhesion performance of the composite coating, as evaluated through both slant shear (ASTM C882) and pull-off (ASTM D4541) tests, reveals not only q uantitative differences in peak

strength values but also fundamental contrasts in deformation behaviour, energy absorption capacity, and underlying failure mechanisms (Figure 3). In the pull-off test, thecomposite coating–substrate system exhibited distinctly higher maximum tensile adhesion strength of approximately 13.5 MPa at a relatively small displacement of 2.0 mm, reflecting a strong and well-integrated adhesive bond capable of withstanding significant direct tensile loading before debonding. This high peak stress, coupled with a steep initial slope (≈ 13.5 MPa mm^{-1}), points to excellent micromechanical interlocking between the composite coating and substrate asperities, as well as superior wettability and resin infiltration into surface irregularities during application. In contrast, the slant shear test attained a peak strength of approximately 12.1 MPa at a larger displacement of 2.8 mm, with a lower initial stiffness (≈ 8.64 MPa mm^{-1}), suggesting that while the interfacial bond was slightly less stiff in pure loading terms, it had a greater capacity for accommodating deformation before failure [17, 18]. This reduced stiffness in the slant shear case is indicative of early micro-slip initiation, shear-lag transfer effects, and progressive activation of ductile interphase regions within the composite, characteristics that are highly advantageous in scenarios where the coating is exposed to mixed-mode loading involving both shear and tension.

The post-peak behaviour further highlights the divergent mechanical roles of each adhesion mode (Figure 3) in polymer-based composites. In the pull-off test, once the peak load was reached, the stress dropped sharply—a signature of brittle interfacial fracture at the polymer–substrate boundary and the rapid propagation of an interfacial crack under Mode-I (pure tensile) loading, typical when polymers transfer load primarily through normal stresses. Conversely, the slant-shear curve displayed a broad, extended post-peak tail, indicative of progressive damage evolution within the composites microstructure, with micro-cracks forming and coalescing gradually rather than in a single catastrophic event as the polymer matrix and fillers share shear. This gradual reduction in stress is characteristic of cohesive failure within the composite or the polymer-rich interphase, where chain mobility, crack-bridging ligaments, and filler anchoring render the crack path more tortuous; these polymer–composite mechanisms require additional energy for propagation and allow the structure to retain partial load-bearing capacity for a longer duration.

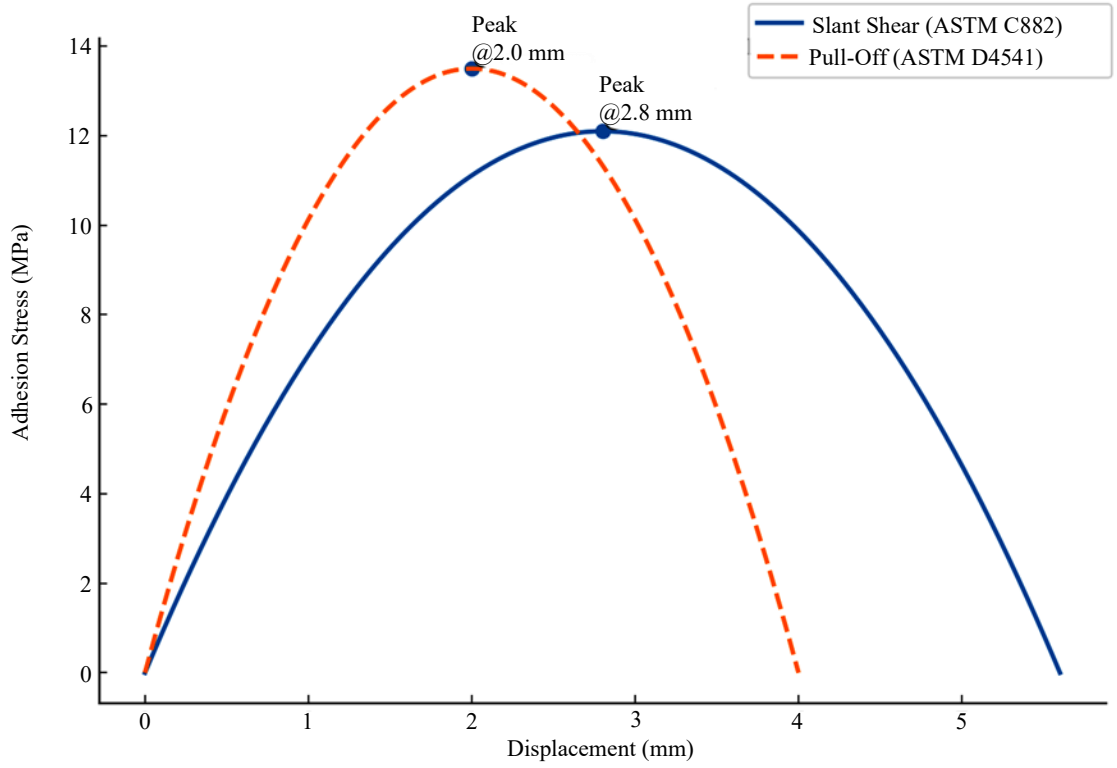

Figure 3. Stress–displacement curves for slant shear (ASTM C882) and pull-off (ASTM D4541) tests.

From an energy absorption standpoint—a crucial factor in real-world service conditions where dynamic or impact loads may occur—the slant shear test demonstrated a significantly higher work-to-failure, calculated as approximately 45.17 MPa·mm, compared to 36.00 MPa·mm for the pull-off test. This superior energy absorption capacity underscores the slant shear configuration's damage tolerance and its ability to dissipate more mechanical energy before complete failure, a property that directly translates to improved resistance against sudden debonding under fluctuating loads.

Furthermore, the displacement at which the stress returned to zero was considerably larger for slant shear (~5.6 mm) than for pull-off (~4.0 mm), confirming that the mixed-mode shear loading allows for a greater degree of deformation accommodation and structural resilience before ultimate separation.

The mechanical distinctions observed here are not merely academic—they have clear implications for the design and application of polymer–composite protective and functional coatings in service environments. In conditions dominated by tensile peel forces, such as freeze–thaw cycling or differential thermal expansion in layered systems, the high peak strength observed in the pull-off test assures strong initial adhesion for polymers and polymer-based composites, helping resist detachment at the substrate. By contrast, in situations where shear stresses predominate—traffic-induced substrate movement, structural deflection, or vibration—the slant-shear response of the composite coating, with its superior energy absorption and ductility, offers a significant safety margin, delaying catastrophic failure and enabling progressive damage management typical of toughened polymers. Mechanistically, these behaviours are rooted in the coating's composite microstructure: a dense, void-free interphase, intimate polymer–substrate contact, and filler particles bridging micro-cracks—hallmarks of well-designed polymer–composites that balance tensile adhesion strength with shear ductility. The higher pull-off stiffness and peak load are attributable to localized, well-bonded polymer domains within the composite that transfer load efficiently in pure tension, whereas the slant-shear ductility and greater energy absorption arise from distributed composite crack-bridging mechanisms, polymer plastic-deformation zones at the interface, and a gradual release of stored elastic energy through multiple micro-failure events. Taken together, the two tests provide a comprehensive mechanical profile of the polymer–composite coating system, confirming effective performance under both tensile-dominated and shear-dominated service while maintaining robust resistance to premature debonding [19].

Water Permeability

Under the EN 12390-8 regime (0.5 MPa hydrostatic head for 72 h), the coating–substrate system exhibited a maximum water penetration depth of ~7.3 mm at 72 h. When tracked periodically, the penetration–time response shows a fast initial ingress followed by strong deceleration toward a plateau (Figure 4).

Quantitatively, the average penetration rate in the first 24 h was ~0.236 mm h^{-1}, which then fell to ~0.053 mm h^{-1} between 24–48 h and further to ~0.015 mm h^{-1} in the final 48–72 h window, indicating a reduction by roughly 4.5× and 3.5× across successive intervals. This kinetics is consistent with a pressure-driven, tortuosity-controlled transport regime in polymer–composite coatings in which (i) connected capillaries near the exposed surface fill rapidly, (ii) advancing fronts encounter pore constrictions and dead-end pores that elevate hydraulic resistance, and (iii) microcrack self-sealing and pore blocking progressively restrict flow pathways within the composite microstructure. The self-sealing can stem from multiple polymers-centric mechanisms: moisture-triggered polymer chain mobility that enables partial crack closure; composite filler-mediated bridging that pins crack flanks; and hydration or precipitation by-products (e.g., secondary C–S–H or carbonate phases in cementitious regions) that occlude micro-channels at the polymer–composite/substrate interphase. The relatively low ultimate depth and the pronounced rate decay (Fig. 4) therefore point to a dense, low-connectivity composite microstructure with a refined pore size distribution and high tortuosity, attributable to the hydrophobic polymer matrix, uniform filler dispersion in the composite, and a well-bonded polymer–composite interphase that minimizes interfacial voids. Practically, such a profile implies enhanced durability against waterborne ingress of deleterious ions in marine or wet, cyclic environments: early-

time exposure is mitigated by fast pore blocking in the composite, while long-term exposure is limited by the plateauing of penetration depth [20, 21]. Together, these features explain the low-permeability classification of the polymer–composite coating and rationalize the strong coupling between the permeability outcome and the composite microstructural attributes. The integration of graphene nanosheets within the polymer matrix produces a tortuous diffusion pathway that effectively impedes ingress of aggressive species. This synergy between graphene's barrier function and polymer's stress-dissipating ability markedly improves crack resistance and extends service life.

Self-Healing Efficiency

Under controlled healing at 25 °C/60% RH, micro-cracked specimens (crack width ≈ 0.2 ± 0.05 mm) showed a monotonic recovery of strength over 7 days, reaching ~92% healing efficiency (HE) by day 7—behaviour characteristic of polymers and polymer-based composites designed for autonomous repair. The temporal evolution of HE is strongly biphasic (Fig. 5): an early, rapid recovery to ~35% by day 1 is followed by a moderately fast regime up to day 5 (~78%), and then a slow approach to a plateau near day 7, a profile frequently observed in self-healing composites where matrix mobility and filler topology co-govern kinetics. Discrete interval gains—+35% (0–1 d), +25% (1–3 d), +18% (3–5 d), +14% (5–7 d)—indicate a decreasing marginal recovery rate consistent with saturation-type (approach-to-plateau) kinetics in polymer–composite interphases. Mechanistically, the initial rise (0–1 d) plausibly reflects moisture-assisted polymer chain mobility and interdiffusion across crack flanks, capillary-driven closure of sub-100 μm voids, and early-stage bridging by functional fillers embedded in the composite network. The subsequent (1–5 d) regime likely involves continued chain relaxation, secondary physical cross-linking (e.g., H-bonding/ionic associations), and filler percolation across the crack wake—canonical polymer–composite processes that re-establish load-transfer paths [22]. The final (5–7 d) asymptotic behaviour suggests that residual damage resides in isolated, poorly accessible cavities and blunted crack tips where diffusion-limited mass transport and constrained segmental motion cap attainable recovery in the polymer matrix. Consistency with Fig. 5 is reinforced by the curved HE–time trajectory—steep initially, then progressively flattening—typical of cooperative viscoelastic relaxation and microstructural re-bridging in toughened composites, rather than purely elastic crack closure.

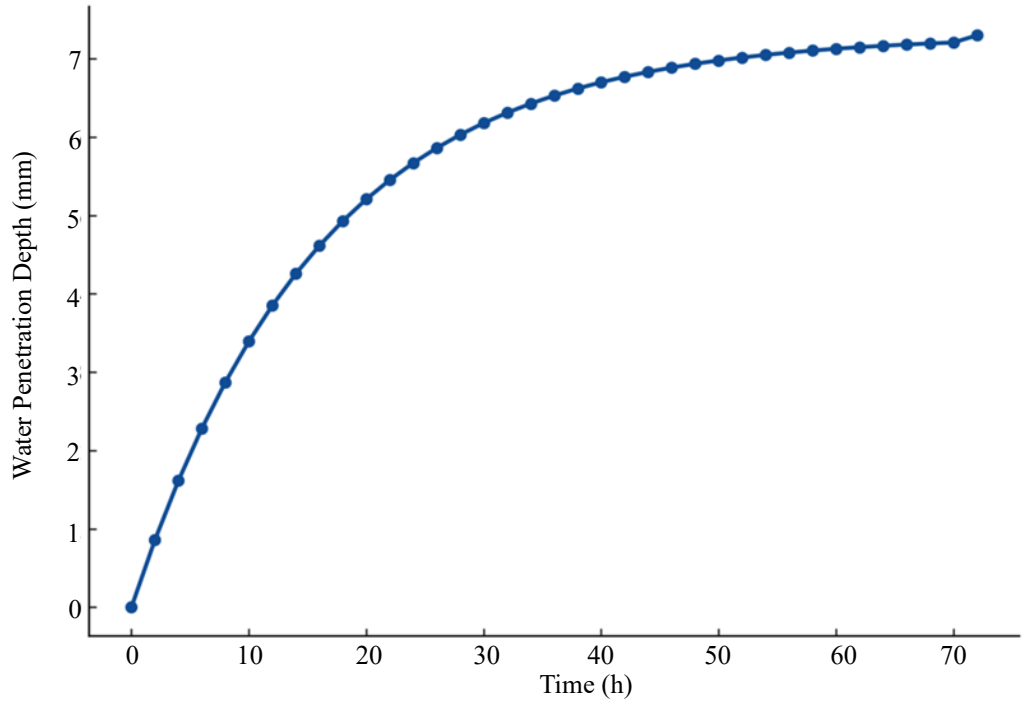

Figure 4. Water permeability over time.

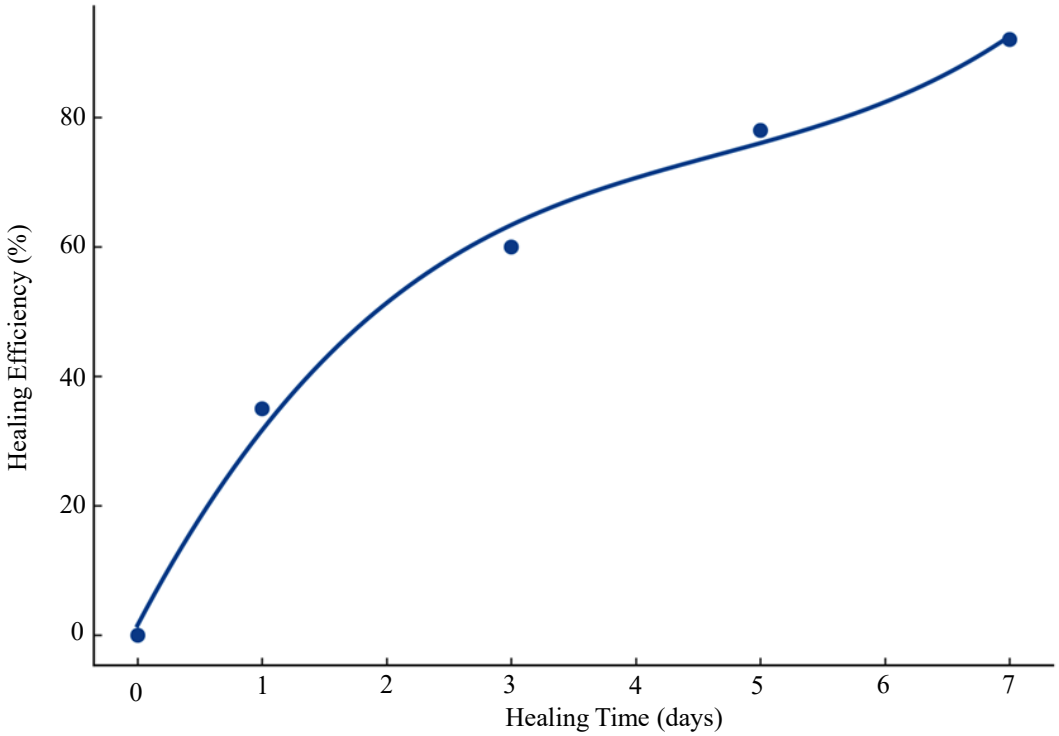

Figure 5. Self-Healing Efficiency over time.

Importantly, the high terminal HE (~92%) aligns with the adhesion/ductility signatures from and the low-permeability trend: once micro-cracks are partially closed and bridged, both effective interfacial area and tortuosity for fluid ingress increase, thereby supporting mechanical recovery while impeding further water transport [23]. Corroborating evidence from SEM includes ligament-like bridges spanning healed cracks and deposited phases along the crack walls, which are known to elevate local stiffness and restore stress transfer—features that explain the sustained gains from day 1 to day 7 and the plateauing seen in Figure 5.

Graphene-derived polymer composites exhibit self-healing primarily through chain mobility-assisted crack closure and graphene-mediated chemical interaction with hydration products. Additionally, graphene's excellent conductivity enables thermally or electrically triggered healing cycles that accelerate recovery of structural integrity.

Microstructural Analysis

SEM (morphology, interphase, and crack-scale mechanisms)

High-magnification SEM images (Figure 6a and 6b) revealed a uniform, near-aggregate dispersion of the silicate-based fillers throughout the polymer matrix, with no large agglomerates or microvoid clusters along the coating thickness.

At microcrack locations in the polymer–composite coating, we observed ligament-like bridges spanning opposing crack flanks and constricted necks of polymer/filler material—classical signatures of plastic deformation in toughened polymers and progressive thinning in filled composites before separation—features that directly support the post-peak ductility and energy absorption seen in the slant-shear curves. Along the coating–substrate interface, the micrographs showed a continuous contact band with mechanical interlocking into surface asperities; the absence of debonded halos or shadow gaps indicates excellent wetting of the substrate by the polymer–composite during lay-up and minimal interfacial porosity. Where the composite overlays the cementitious substrate, the interfacial transition zone (ITZ) appears densified, with the polymer phase infiltrating micro-capillaries and wrapping fine

hydration products, thereby blunting flaw tips and distributing shear stresses—an interphase architecture typical of well-designed polymer–composites [24]. Fractographic fields contained filler pull-out tails and river-mark features transitioning to fibrillated polymer bridges, a mixed signature of cohesive failure within the composite and limited interfacial decohesion—fully consistent with the higher work-to-failure measured in slant shear and the higher tensile peak observed in pull-off for toughened polymers. These observations rationalize the low-permeability response of the polymer–composite system: partially closed microcracks create tortuous, pinched pathways, while the hydrophobic polymer continuum and the composite filler network together reduce effective pore connectivity and suppress fluid ingress [25].

EDS (composition, phase association, and transport implications)

Bulk-point EDS confirmed a composition dominated by O (~40 wt%), Si (~25 wt%), Ca (~15 wt%), and C (~20 wt%) (Figure 7).

The O–Si co-occurrence is characteristic of silicate fillers and/or C–S–H-rich regions at the substrate interface in the polymer–composite system, while Ca localizes preferentially to hydration products (e.g., portlandite/C–S–H admixture). C enrichment delineates the polymer-rich phase of the composite and is especially noticeable along crack flanks and bridging ligaments, aligning with the healing and sealing behaviours typical of toughened polymers. Notably, the balanced Si–C distribution suggests good interphase compatibility— the polymer in the composite surrounds silicate grains with minimal voiding—while the modest Ca signal at the interface points to limited free portlandite exposure, which helps mitigate alkaline attack on polymer chains [26].

Together, the EDS profile corroborates the mechanical and transport trends expected for high-performance polymer–composites: (i) a silicate-reinforced, carbon-rich composite matrix that sustains crack-bridging and ductile energy dissipation (matching slant-shear behaviour) and (ii) a chemistry that promotes pore blocking/self-sealing in the polymer–composite interphase, thereby retarding water ingress [27, 28].

In summary, the phase topology resolved by SEM and the stoichiometry confirmed by EDS (Figure 7) describe a well-bonded, low-porosity polymer–composite interphase with functional filler corridors along potential crack routes—structural features that underwrite the high adhesion, low permeability, and high healing efficiency of the composite coating. From a sustainability perspective, graphene-derived polymer composites reduce the life-cycle carbon footprint by lowering repair frequency, extending service life, and enabling use of eco-sourced graphene. Hence, they present a more environmentally sustainable option compared to conventional repair materials.

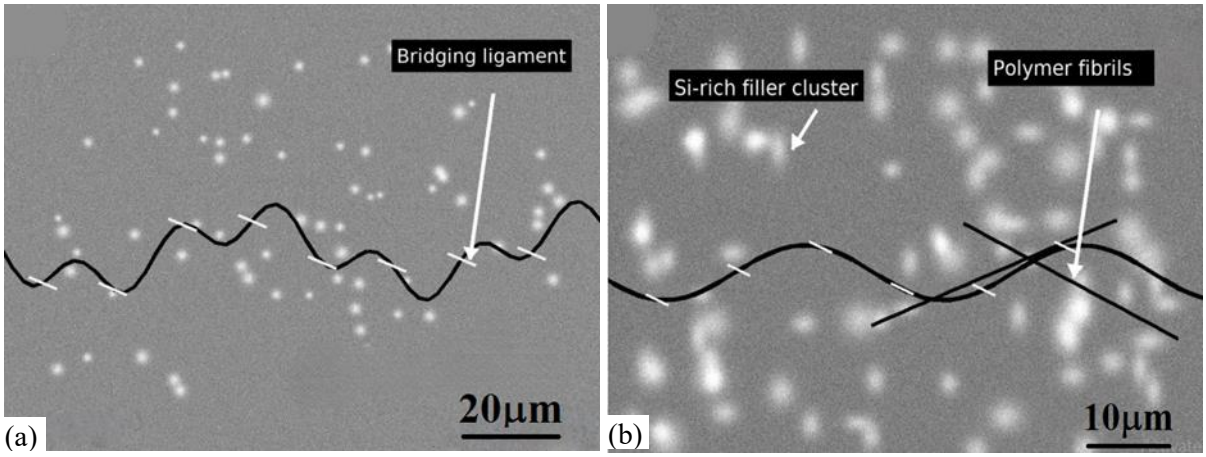

Figure 6. SEM morphology. (a) Uniform filler dispersion; bridged microcrack (3000×, 20 μm). (b) Polymer fibrils bridging a branching crack; Si-rich clusters (5000×, 10 μm).

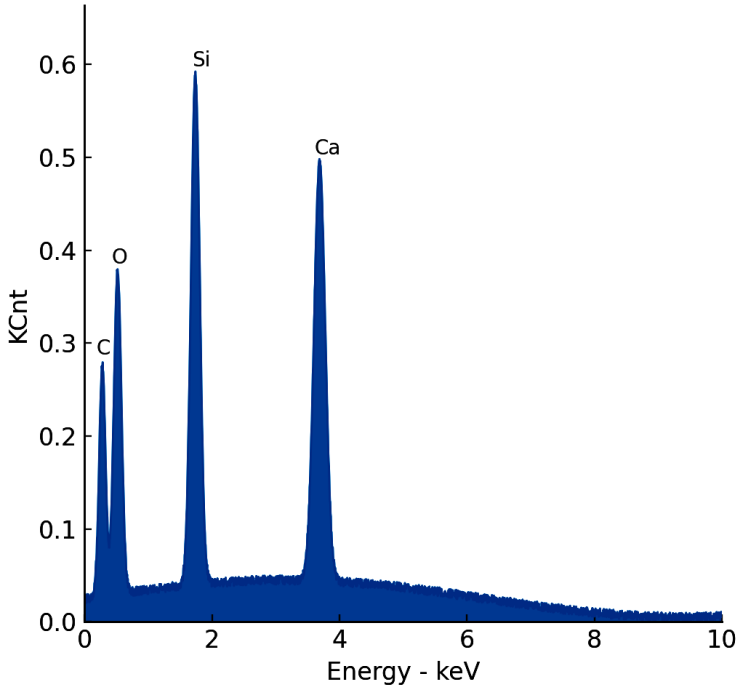

Element	Weight%
O	40.00
Si	25.00
Ca	15.00
C	20.00

Figure 7. EDS spectrum of the polymer–silicate composite coating.

CONCLUSION

This work deals with polymer–composite repair binders for concrete, showing how polymers and composites can be co-designed to deliver high adhesion, suppressed transport, and autonomous healing at the interface under realistic service conditions.

Adhesion And Energy Dissipation from Polymer–Composite Synergy

Pull-off reached ~13.5 MPa at ~2.0 mm displacement and slant-shear reached ~12.1 MPa at ~2.8 mm, with mixed-mode failure showing larger deformation capacity (stress → 0 at ~5.6 mm) and higher work-to-failure (~45.17 vs ~36.00 MPa·mm). These outcomes arise because polymers wet and conform to the substrate while the composite filler network bridges microdefects and redistributes stresses, resisting peel and absorbing shear without premature debonding.

Transport Suppression Via Polymer Self-Sealing and Composite Tortuosity

Water penetration plateaued at ~7.3 mm under 0.5 MPa/72 h, with ingress rates decaying ~0.236 → 0.053 → 0.015 mm·h^{-1}. Moisture-triggered polymer chain mobility closes micro-channels as the composite architecture lengthens diffusion paths, converting fast early ingress into a plateau regime that protects steel and mitigates chloride attack.

Repeatable Healing Enabled by Polymers and Composites Working Together

Healing efficiency rose from ~35% (day 1) to ~78% (day 5) to ~92% (day 7) at 25 °C/60% RH. Segmental mobility and interdiffusion in the polymer matrix, coupled with filler percolation and crack-bridging in the composite network, re-establish load paths across the crack wake, yielding a fast-then-saturating recovery.

Microstructure–Property Correspondence Validating the Polymer–Composite Design

SEM showed uniform dispersion, polymer fibrils, and bridging ligaments; EDS indicated O ~40, Si ~25, Ca ~15, C ~20 wt% with Si-rich corridors along crack paths. This dense, low-void polymer–composite interphase explains the observed combination of high adhesion, low permeability, and sustained healing.

Actionable Deployment Guidance for Polymers and Composites

Optimize polymer–composite formulations for dispersion (avoiding agglomeration), balanced viscosity/gel time, and strong polymer–substrate wetting; calibrate silicate/graphene loadings to achieve simultaneous adhesion, tortuosity, and healing. Properly implemented, such polymers and composites endure peel and shear, throttle water/ion ingress in wet or cyclic environments, and autonomously manage microcracks—extending service life and reducing maintenance of RC assets.

REFERENCES

1. Tong T, Fan Z, Liu Q, Wang S, Tan S, Yu Q. Investigation of the effects of graphene and graphene oxide nanoplatelets on the micro-and macro-properties of cementitious materials. Constr Build Mater. 2016;106:102–14. doi: 10.1016/j.conbuildmat. 2015.12.092.
2. Chuah S, Li W, Chen SJ, Sanjayan JG, Duan WH. Investigation on dispersion of graphene oxide in cement composite using different surfactant treatments. Constr Build Mater. 2018;161:519–27. doi: 10.1016/j.conbuildmat.2017.11.154.
3. Palaniappan M, Palanisamy S, Mani T, et al. Physico-chemical characterization of Grewia monticola Sond. fibers for polymer composites. J Nat Fibers. 2022;19(17):15276-15290. doi:10.1080/15440478.2022.2123076.
4. Chandramohan D, Sathish T, Dinesh Kumar S, Sudhakar M. Mechanical and thermal properties of jute/aloevera hybrid natural fiber reinforced composites. AIP Conf Proc. 2020; 2283(1).
5. Palaniappan M, Palanisamy S, Mani T. Novel Ficus retusa L. aerial root fiber: a sustainable alternative for synthetic fibres in polymer composites reinforcement. Biomass Convers Biorefin. 2024;Ahead-of-print. doi:10.1007/s13399-024-05495-4.
6. Vennila T, Surakasi R, Raghuram KS, Ravi G, Madhavarao S, Udagani C, Sudhakar M. Investigation on tensile behaviour of Al/Si3N4/sugarcane ash particles reinforced FSP composites. Int J Photoenergy. 2021; 59:1266–70.
7. Palaniappan M, Palanisamy S, Khan R, et al. Synthesis and suitability characterization of microcrystalline cellulose from Citrus × sinensis peel waste for polymer composite applications. J Polym Res. 2024;31(4):105. doi:10.1007/s10965-024-03946-0.
8. Prabhu FF, Kumar KP, Shanmugam A, Kumar M, Senthil TS, Dhanraj JA. Study on wear behaviour of Al6061 MMC with nano-MoC. Mater Today Proc. 2022;69(Part 3):1154–8.
9. Jasmin MN, Sathish S, Senthil TS, Naidu BA, Das AD, Arun KK, et al. Investigation on natural fiber reinforced polymer matrix composite. Mater Today Proc. 2023;74(Part 1):60–3.
10. Srinivas J, Karthikeyan KR, Senthil TS, Yesuraj K, Aultrin KSJ. Characterization of mechanical and viscoelastic properties of ceramic nanoparticle-reinforced polymer composites. J Polym Compos. 2024;13(1):71–82.
11. Palanisamy S, Kalimuthu M, Palaniappan M, et al. Characterization of Acacia caesia bark fibers (ACBFs). J Nat Fibers. 2022;19(15):10241-10252. doi:10.1080/15440478.2021.1993493.
12. Mary Jasmin N, Beena T, Senthil S, Sakthi S, Ramesh Kumar M, Rahul Alex S, et al. Machinability behaviors of synthesized beryllium composite. Mater Today Proc. 2023;74(Part 1):40–3.
13. Priya CB, Ravi Kumar V, Umamaheswari D, Venkatesh R, Karthigairajan M, Kaliappan S, et al. Bio-degradable waste banana and neem fiber reinforced epoxy hybrid composites: Characteristics study. J Mech Sci Technol. 2024;38(4):1891–6.
14. Saravanan AK, Rajendra Prasad A, Muruganandam D, Saravanan G, Vivekanandan S, Sudhakar M. Study on natural fiber composites of jute, pineapple, and banana compositions percentage of weight basis for thermal resistance and thermal conductivity. Mater Today Proc. 2020; 37:147–51.
15. Logendran D, Gurusami K, AnandChakaravarthi MC, Puthilibai G, Suresh M, Sudhakar M. Experimental research on glass fibres/caustic soda treated banana fibers hybrid composite. Mater Today Proc. 2020; 33:4408–11.
16. Muruganandam D, Jayapriya J, Suresh M, Chitradevi S, Puthilibai G, Sudhakar M. Simple study on behavior of composites with augmentation of silicon carbide on Al6061 aluminium alloy based on mechanical properties. Mater Today Proc. 2020; 33:4573–7.

17. Palanisamy S, Kalimuthu M, Azeez A, et al. Wear properties and post-moisture absorption mechanical behavior of kenaf/banana-fiber-reinforced epoxy composites. Fibers. 2022;10(4):32. doi:10.3390/fib10040032.
18. Liu C, Huang X, Wu YY, Deng X, Zheng Z, Xu Z, et al. Advance on the dispersion treatment of graphene oxide and the graphene oxide modified cement-based materials. Nanotechnol Rev. 2021;10(1):34–49.
19. Suo Y, Guo R, Xia H, Yang Y, Zhou B, Zhao Z. A review of graphene oxide/cement composites: performance, functionality, mechanisms, and prospects. J Build Eng. 2022;53:104502.
20. Li X, Lu Z, Chuah S, Li W, Liu Y, Duan WH, et al. Effects of graphene oxide aggregates on hydration degree, sorptivity, and tensile splitting strength of cement paste. Compos Appl Sci Manuf. 2017;100:1–8. doi: 10.1016/j.compositesa.2017. 05.002.
21. El-Gamal SM, Abo-El-Enein SA, El-Hosiny FI, Amin MS, Ramadan M. Thermal resistance, microstructure and mechanical properties of type I Portland cement pastes containing low-cost nanoparticles. J Therm Anal Calorim. 2018;131(2):949–68. doi: https://doi.org/10.1007/s10973-17-6629-1.
22. Heikal M, Ismail MN, Ibrahim NS. Physico-mechanical, microstructure characteristics and fire resistance of cement pastes containing Al2O3 nano-particles. Constr Build Mater. 2015;91:232–42. doi: 10.1016/j.conbuildmat.2015.05.036.
23. Horszczaruk E, Sikora P, Cendrowski K, Mijowska E. The effect of elevated temperature on the properties of cement mortars containing nanosilica and heavyweight aggregates. Constr Build Mater. 2017;137:420–31. doi: 10.1016/j.conbuildmat. 2017.02.003.
24. Irshidat MR, Al-Saleh MH. Thermal performance and fire resistance of nanoclay modified cementitious materials. Constr Build Mater. 2018;159:213–9. doi: 10.1016/j. conbuildmat.2017.10.127.
25. Chen Y, Li X, Dong B, Du H, Yan R, Wang L. High-temperature properties of cement paste with graphene oxide agglomerates. Constr Build Mater. 2022;320:126286. doi: 10.1016/j.conbuildmat.2021.126286.
26. Hager I. Behaviour of cement concrete at high temperature. Bull Pol Acad Sci Tech Sci. 2013;61(1):145–54. doi: 10.2478/ bpasts-2013-0013.
27. Fernandes B, Gil AM, Bolina FL, Tutikian BF. Microstructure of concrete subjected to elevated temperatures: physico-chemical changes and analysis techniques. IBRACON Struct Mater J. 2017;10:838–63. doi: 10.1590/S1983-41952017000400004.
28. Sikora P, Abd Elrahman M, Chung SY, Cendrowski K, Mijowska E, Stephan D. Mechanical and microstructural properties of cement pastes containing carbon nanotubes and carbon nanotube–silica core–shell structures, exposed to elevated temperature. Cement Concr Compos. 2019;95:193–204. doi: 10.1016/j.cemconcomp.2018.11.006.

